

# Adaptive ocean gradient tracking using an autonomous underwater vehicle with a boundless model

---

**Tore Mo-Bjørkelund**

Department of Marine Technology

Norwegian University of Science and Technology

Trondheim, Norway

[tore.mo-bjorkelund@ntnu.no](mailto:tore.mo-bjorkelund@ntnu.no)

**Renato Mendes**

Underwater Systems and Technologies Laboratory (LSTS), University of Porto

Porto, Portugal

CoLAB +ATLANTIC

Matosinhos, Portugal

[renato.mendes@colabatlantic.com](mailto:renato.mendes@colabatlantic.com)

**Francisco López-Castejón**

Cartagena Oceanographic Research Institute

and

Universidad Politécnica de Cartagena

Cartagena, Spain

[francisco@cori.institute](mailto:francisco@cori.institute)

**Martin Ludvigsen**

Department of Marine Technology

Norwegian University of Science and Technology

Trondheim, Norway

and

Arctic Technology Department

University Centre in Svalbard (UNIS)

Longyearbyen, Norway

[martin.ludvigsen@ntnu.no](mailto:martin.ludvigsen@ntnu.no)

## Abstract

<sup>1</sup>This work presents a method for exploring a dynamic river plume boundary using an autonomous underwater vehicle with an on board lightweight *boundless* model. *In-situ* decision  
<sup>2</sup>

making enables targeted sampling of the ocean-river plume interaction. The data driven and adaptive approaches affords the capability and opportunity to fully utilize the operational window of operations for the vehicle. The method was developed using a simulated plume and vehicle, and results from simulation studies and successful field trials from the Douro River plume outside Porto, Portugal are presented. The vehicle adapts its path based on underway real-time assimilation of measurements, seeking to gain new information while not straying away from the front. Owing to the unpredictable shape and size of the river front, a model based *boundless* method for adaptive sampling was constructed, generating potential waypoints as a function of the vehicle's position and the accumulated knowledge of the plume. Not bounding the spatial extent of the method allows for great variation in plume shape and size. The boundless models avoids the requirement for a defined operational area over the entire possibility space over river plume realizations, and the need to explore this space. In the method, the depth of the sharpest vertical salinity gradient, or plume depth, is estimated using a two-dimensional *Gaussian Process*, where the plume depth is estimated from a dive and ascent envelope of the robot, traversing the ocean in an undulating fashion. Computational efficiency is gained from the resulting low number of measurements, compared to the number of salinity measurements, and ensuring rapid on board adaption. The next waypoint is chosen as the first waypoint in a path that maximizes the weighted sum of uncertainty, estimated plume depth, and the absolute value of the difference between the current plume depth and the estimated river plume depth along the path. This encourages traversal of the plume in a fashion that enable the extent of the plume to be resolved in high detail. The data driven method was field verified in the Douro river proving the ability to track the the river plume being able to balance exploration and exploitation behavior to maximize the information value of the mission in real time onboard the vehicle.

28 **1 Introduction**

29 **1.1 Ocean fronts**

30 An ocean front is a boundary between two water masses with distinct properties, making them distinctly  
31 separable from each other. This phenomenon can occur at vastly different scales, ranging from open ocean  
32 mesoscale fronts, to tiny river fronts at estuaries. The name "front" refers to a wartime front between  
33 two armies, a near-static border where intense exchange takes place. The more peaceful exchange of salt,  
34 temperature, nutrients, and biomass between ocean fronts is a dynamic environment driven by currents,  
35 wind, gravity, density, and waves. Ocean fronts are limited in their extent, dynamic in location and severity,  
36 and are regions of interest for oceanographic, biogeochemical, and biological phenomena [1, 2], and mapping  
37 and monitoring them, adaptive missions have a large potential for optimizing the data acquisition. River  
38 plumes in the ocean are buoyant fronts with limited spatial extent and dynamics, as it is bound to the  
39 shore at the estuary. They can be defined by a water mass from the river outflow that enters a surrounding  
40 ambient water-mass. The biogeochemical pathways taking place at the interface between these different  
41 waters have a direct impact on fisheries and pollution dispersion [1, 2, 3], as well as primary production  
42 and heat exchange. River plumes or fronts are usually studied with numerical models, satellite imagery, *in*  
43 *situ* water sampling, or conducting sensor-based casts from a human-crewed vessel. The use of Autonomous  
44 Underwater Vehicles (AUVs) can improve spatial and temporal resolutions but deterministic mission plans  
45 rely on accurate knowledge of the front and in an environment as dynamic as a river plume it is challenging.  
46 Most satellite images are affected by cloud coverage, and satellite imagery taken once a day has poor temporal  
47 and spatial resolutions. Further, remote sensing products only provide a snapshot of a 2D characterization  
48 of the surface plume, providing little information about the water-column [4, 5, 6].

49 **1.2 Underwater adaptive sampling**

50 Adaptive sampling using AUVs has become more commonplace in the last decade [7, 8, 9, 10, 11, 12, 13,  
51 14, 15, 16, 17]. These methods can be divided into two categories, *subsumption-based* [18] and *deliberative*  
52 [19, 13] methods. Whereas subsumption-based methods will act as a finite state machine and act according to  
53 a set of triggers and responses [20], the deliberative method compares and evaluates the potential outcomes  
54 of different choices based on a utility function. In deliberative methods, a model is required to predict the  
55 environment, such as Gaussian Processes (GP) [21] or a higher order simulation model [22] upon the utility  
56 can be extracted based on location, time and value. With such a model in place, one can deliberate upon

57 potential paths according to their score based on a defined utility or evaluation function.

58 Path planning algorithms are often limited by an exponential combinatoric increase in dimensionality [23]  
59 due to the exponential growth of combinations as the planning horizon is expanded. Therefore, the problems  
60 are often simplified using heuristics and/or greedy algorithms [13]. In underwater adaptive sampling, GP  
61 modeling has shown to be a suitable tool for modelling the marine environment [24, 12] at high spatiotemporal  
62 resolution over submesoscale volumes. With operating speeds greater than gliders and Remotely Operated  
63 Vehicles (ROVs), AUVs are suited for studying dynamic ocean phenomena such as fronts, gradients and  
64 plumes. However, as fronts can be challenging to locate precisely, and a preprogrammed mission would most  
65 likely capture more redundant and less interesting data than an adaptive mission where the vehicle can plan  
66 its path [25]. Our goal is to provide measurements of the distribution of water masses in a river plume  
67 adaptively and efficiently. The system measure gradients of salinity and temperature, and uses the salinity  
68 to estimate the river plume depth and to adapt the vehicle path. Both the vertical and horizontal vehicle  
69 paths are adapted, independently of each other. The vertical component of the trajectory is adapted using  
70 the estimated river plume depth at the current location, attempting to cross the maximal gradient at each  
71 dive and ascent. The horizontal path is adapted to explore and map the river plume based on the on-board  
72 model of its severity and extent. Previous GP models of ocean parameters have attempted to evaluate the  
73 model on a predefined grid [13, 12, 16]. Here, a gridless approach is used, to free the robot from preconceived  
74 notions about plume shape, enabled by sparsity in model and path planning. By decoupling the vertical and  
75 horizontal models, the method permits interchangeability and specification depending on the vertical and  
76 horizontal features of interest. The on board model is lightweight, enabling embedded integration on most  
77 crafts, and delivering real time decision making and planning.

78 **2 Method**

79 The algorithm consists of five parts: 1) the initial pilot-survey, 2) the river plume depth measurement, 3) the  
80 GP-model, 4) the potential paths, and 5) the evaluation of the potential paths. In this section, we present  
81 each part and how they fit together to complete the river plume tracking task. The plume tracking mission  
82 consists of two phases: the pilot survey and the adaptive phase. The pilot survey [12] is a pre-programmed  
83 transect, long enough to build a model, and the adaptive phase is similar to an explore/exploit structure  
84 [13]. The pilot survey is designed beforehand as a preliminary salinity data gathering mission, and the  
85 adaptive phase starts automatically after the pilot survey. During the mission, the vehicle will travel in an  
86 undulating see-saw, or yoyo-pattern, and adapt the amplitude and vertical profile of the vehicle path. The  
87 horizontal path is adapted independently of the vertical for each new estimate of the plume depth. The  
88 vehicle undulates between the surface and the maximum mission depth for the pilot survey, and dynamically  
89 in the adaptive phase according to the underway measurements. The horizontal waypoints of the vehicle  
90 will be updated at each *update step*; these happen for every half vertical path cycle. At the *update step*, the  
91 model of the environment and the desired waypoint is updated based on the new measurements, and the  
92 best fitting horizontal path is derived. A flow-chart overview of the adaptive phase is presented in Figure 1.

93 **2.1 Prior**

94 The prior consists of the operator inputs, as described below, and the data from the pilot survey. It generates  
95 the necessary input for the adaptive phase, the core function for horizontal adaptive behavior. Contextual  
96 data from the operators, thresholds, heuristics and operational variables, and input data to the adaptive  
97 phase are all part of the prior knowledge, constraining and shaping the adaptive phase.

98 **Operator inputs**

99 The adaptive planning algorithm depends of the operator prior inputs and are as follows:

- 100 • Minimum ocean salinity,  $s_o$ , if the salinity is above this value, it is considered oceanic.  
101 • Maximum river salinity,  $s_r$ , if the salinity is below this value, it is defined to be river water.  
102 • Max depth,  $d_{max}$ , the maximal depth allowed for the mission.  
103 • Mission duration, as the adaptive mission can go on for ever, we can end it after a desired time has  
104 passed.

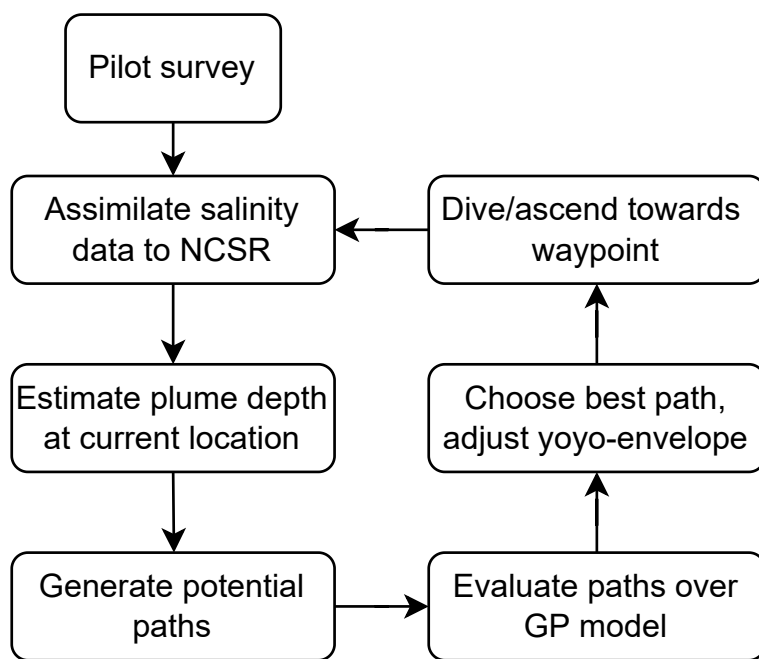


Figure 1: A flowchart representation of the adaptive phase. With the main components of a dive and ascent envelope and an overview of the processes in the adaptive waypoint tracking.

- 105     • Starting position,  $p_{start} = [\text{lat}_{start}, \text{lon}_{start}]$ , where the pilot survey begins.
- 106     • Pilot survey length,  $l_{ps}$ , the length of the two transects in the pilot survey, must be long enough to  
107        cross in to the plume.
- 108     • Pilot survey orientations,  $[\theta_0, \theta_1]$ , the orientation of the two pilot survey transects.

109 With these inputs from the operator, the pilot survey can start.

110 **Pilot survey**

111 The pilot survey provides data to build a model of the river plume using a GP. The longer the survey, the  
112 more measurements the initial  $\ell$ GP will be based on. Starting at  $p_{start}$ , the pilot survey traverses a length  
113  $l_{ps}$  in direction  $\theta_0$ , then a length  $l_{ps}$  in direction  $\theta_1$ . During the pilot survey, the vehicle will travel in a  
114 yoyo-pattern between the surface and  $d_{max}$ , collecting salinity data. Each dive and ascent constitutes a  
115 envelope, containing the salinity measurements, depth and position data. Each profile is then analyzed in  
116 the data collection to estimate the river plume depth.

117 **2.2 Data collection**

118 The vertical boundary of river plume is estimated from salinity measurements to reduce the amount of data  
119 input to the GP. This serves two purposes; 1) it removes the vertical dimension from the model, simplifying  
120 it from  $\mathbb{R}^3$  to  $\mathbb{R}^2$  and 2) it reduces the number of samples used to build the GP model. The vertical position  
121 of the river plume boundary,  $d_r$  is estimated by using each vertical salinity profile,  $\mathbf{p} = [\mathbf{s}, d]$ , and filtering  
122 it using the algorithm presented in Equation 1.

$$\hat{d}_r(\mathbf{s}) = \begin{cases} 0 & \text{if } \min(\mathbf{s}) > s_o \\ d_{max} & \text{if } \max(\mathbf{s}) < s_r \\ \underset{d}{\operatorname{argmax}}(|\frac{\partial NCSR(\mathbf{p})}{\partial d}|) & \text{else} \end{cases} \quad (1)$$

123 Where  $NCSR(\cdot)$  is the Natural Cubic Spline Regression of the salinity as a function of depth.

124 **Natural cubic spline regression**

125  $NCSR(\cdot)$  is a method for fitting data to a set of cubic polynomials, defined over an interval of the input  
126 range, with the constraint that they are  $C^2$  continuous and that the double derivative is zero at the ends.  
127 Salinity data collected in the profile is filtered using a  $NCSR(\cdot)$ , the spline is differentiable and suitable for  
128 detecting gradients [26]. The partial  $NCSR(\cdot)$  function is denoted as:

$$S_i(x) = a_i + b_i x + c_i x^2 + d_i x^3 \quad x \in [x_i, x_{i+1}] \quad (2)$$

129 The full  $NCSR(\cdot)$  is then the collection of all  $S_i(x)$  over the input domain, in our case depth,  $[x_{min}, x_{max}]$ ;  
130  $S(x) = [S_0, S_1, \dots, S_{n-1}]$ , where  $n$  is the number of *knots*, or divisions between functions, in the spline. If the  
131 input data set is has size  $m$  and  $n = m$ , the  $NCSR(\cdot)$  perfectly interpolates the data, and in the particular  
132 case of  $n = 1$ , the  $NCSR(\cdot)$  reduces to a cubic polynomial regression. As the purpose of this  $NCSR(\cdot)$  is  
133 to filter the salinity data on the depth axis, it has to have enough knots to capture the features in the data  
134 while still filtering the noise in the data. From previous experience,  $n = 6$  has proved to be sufficient [26] for  
135 salinity and temperature gradients in the ocean sampled along one dimension.

136 **Vertical profile**

137 By using the  $NCSR(\cdot)$  to filter the data, it becomes differentiable, and the river plume depth can be defined  
138 to be the depth of greatest absolute value of the vertical gradient. There can be several water masses within  
139 the boundaries of  $s_o$  and  $s_r$ , the river plume depth is defined as the depth of the maximal absolute gradient  
140 for this work. For illustration, a  $NCSR(\cdot)$  with 6 knots and its differentiation is presented in Figure 2, along  
141 with the input data.

142 **Current plume depth estimate**

143 During the adaptive phase, the model running onboard the vehicle will estimate the vertical boundary of  
144 the plume at the vehicles current position,  $\hat{d}_{rc}$ . This estimation serves two purposes, the first is to adapt  
145 the average depth and amplitude of the yoyo-maneuver used in data collection. The second is to compare  
146 the estimated river plume boundary at the current position with estimates at other locations, such that it  
147 can seek heterogeneity. The former will be presented in this section, along with the method for deciding the

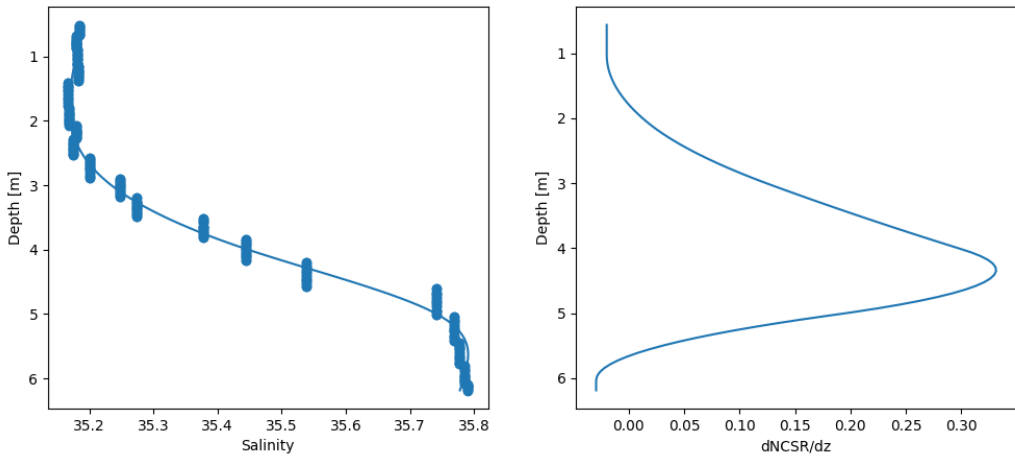


Figure 2: In the left panel, a NCSR over a salinity profile from the field trials is plotted as a continuous line, with the raw data scatter plotted in the same figure. In the right panel, the NCSR is differentiated in order to find the depth of maximum change, between 4 and 5 meters depth in this case.

148 average depth and amplitude of the yoyo, while the latter will be presented in Section 2.5. First, we low-pass  
 149 filter the river plume depth estimates, removing some of the process or measurement noise, as presented in  
 150 Equation 3, where  $k$  is the latest update step, and  $\alpha \in [0, 1]$  is the weight of previous estimates.

$$\hat{d}_{rc}^k = \alpha \hat{d}_{rc}^{k-1} + (1 - \alpha) \hat{d}_r^k \quad (3)$$

151 By using the standard deviation,  $\sigma_f$ , from Equation 10, we center the yoyo-maneuver around  $\hat{d}_{rc}^k$ , and add or  
 152 subtract two  $\sigma_f$ , thereafter we threshold the value between the surface and the maximum depth, as presented  
 153 in Equation 4. A realization of the yoyo-envelope from the field trials is plotted in Figure 10.

$$\text{yo-yo-envelope} = \begin{cases} d_{yo-yo}^{top} &= \max[0, \hat{d}_{rc}^k - 2\sigma_f] \\ d_{yo-yo}^{bottom} &= \min[d_{max}, \hat{d}_{rc}^k + 2\sigma_f] \end{cases} \quad (4)$$

154 **2.3 Spatial model**

155 A GP is used for estimation of the river plume depth and its uncertainty at unmeasured locations. The  
156 evaluation points are generated at each step in the adaptive cycle, as a function of the vehicle position,  
157 freeing the robot from the limitations of a predefined grid. In this case, the prior model and covariance  
158 matrix is generated for each evaluation, in stead of propagating them [22, 27] as they are not readily fixed  
159 in size.

160 **Gaussian Process**

161 *A Gaussian Process is a collection of random variables, any number of which have a joint*  
162 *Gaussian distribution.* - [21]

163 Formally presented as in Equation 5, where  $m_{GP}(\cdot)$  is a de-trending function such that  $\mathbf{d}_r - m_{GP}(\mathbf{x}) \sim$   
164  $\mathcal{N}(0, \sigma_{nf}^2)$  ideally, where  $\mathbf{d}_r$  is the measurement vector,  $\sigma_{nf}^2$  is the variance in the data, and  $\mathbf{k}(\cdot, \cdot)$  is the  
165 kernel function, providing the spatial correlation between the positions  $\mathbf{x}$  and  $\mathbf{x}'$

$$f(\mathbf{x}) = \mathcal{GP}(m(\mathbf{x}), k(\mathbf{x}, \mathbf{x}')) \quad (5)$$

166 A GP can be used to model spatial data with an underlying Gaussian distribution. In the case of the  
167 salinity of the two water bodies, *river plume* and *ocean*, the distribution would most likely be a bimodal  
168 Gaussian. This type of distribution is another reason for choosing river depth as the prediction variable. The  
169 de-trending function,  $m_{GP}(\cdot)$  used in this GP is a linear two-dimensional regression over the data,  $\mathbf{d}_r, \mathbf{X}$ ,  
170 fitted with a least-squares regression. Our GP uses the squared exponential kernel, presented in Equation  
171 6, where  $\sigma_f^2$  is the variance of the data without the nugget effect,  $l$  is the length scale, and  $\mathbf{x}$  and  $\mathbf{x}'$  are  
172 positions.

$$k_{SE}(r) = \sigma_f^2 \exp\left(-\frac{r^2}{2l^2}\right) \quad (6)$$

$$r = |\mathbf{x} - \mathbf{x}'| \quad (7)$$

173 In addition, we add the nugget effect,  $\sigma_n$ , [28], taking measurement and unmeasured process noise into  
174 account. Thus, our kernel becomes  $k(r) = k_{SE}(r)$ .

175 The prediction of the river plume depth,  $\hat{d}_r$ , and its uncertainty,  $\Sigma_r$ , is calculated by the GP as presented  
176 in Equations 8 and 9, where  $\mathbf{y} = \mathbf{d}_r - \mathbf{m}_{GP}(\mathbf{x}')$ ,  $K(\gamma, \xi)$  is the covariance matrices evaluated at locations  
177  $\gamma$  and  $\xi$ , and  $\mathbf{m}_{GP}(\mathbf{x}')$  is the vector of de-trending values evaluated at  $\mathbf{x}'$ .

$$\hat{d}_r = K(\mathbf{x}', \mathbf{x})[K(\mathbf{x}, \mathbf{x}) + \sigma_n^2 I]^{-1}\mathbf{y} + \mathbf{m}_{GP}(\mathbf{x}') \quad (8)$$

$$\Sigma_r^2 = K(\mathbf{x}', \mathbf{x}') - K(\mathbf{x}', \mathbf{x})[K(\mathbf{x}, \mathbf{x}) + \sigma_n^2 I]^{-1}K(\mathbf{x}, \mathbf{x}') \quad (9)$$

178 The measurements,  $\mathbf{d}_r$ , are used to estimate the variance in the data,  $\sigma_f^2$ , at each iteration, using the 20  
179 latest measurements, as presented in Equation 10. In addition, a threshold was introduced in case the last  
180 20 samples were in the open ocean, where  $d_r = 0\text{m}$ , or in the case of a deep river plume where  $d_r = d_{max}$ .

$$\sigma_f = \max \left\{ \begin{array}{l} \sqrt{\frac{1}{20} \sum_{i=N-20}^N (d_{ri} - \bar{d}_r)^2} \\ \sigma_{fmin} \end{array} \right\} \quad (10)$$

181 One underlying assumption is that the vehicle speed is sufficiently large concerning the process dynamics of  
182 such a river plume, which is the reason for the static nature of the spatial model. The same assumptions  
183 have been used by [24], [15] and [12] for similar conditions. A flowchart representation of the GP model and  
184 evaluation is presented in Figure 3, containing the central parts of the model.

## 185 2.4 Path generation

186 In generating the potential path, we seek to achieve three goals; 1) the set of potential paths must be  
187 computationally cheap to evaluate, 2) have a higher resolution closer to the vehicle , and 3) have a directional  
188 component. By limiting the angle between legs in the potential paths, directionality is conserved, and by  
189 generating the waypoints at a higher density close to the vehicle, near-term features can be found and  
190 explored. This enables small detours in the near term while still having a far-off goal in sight by having a

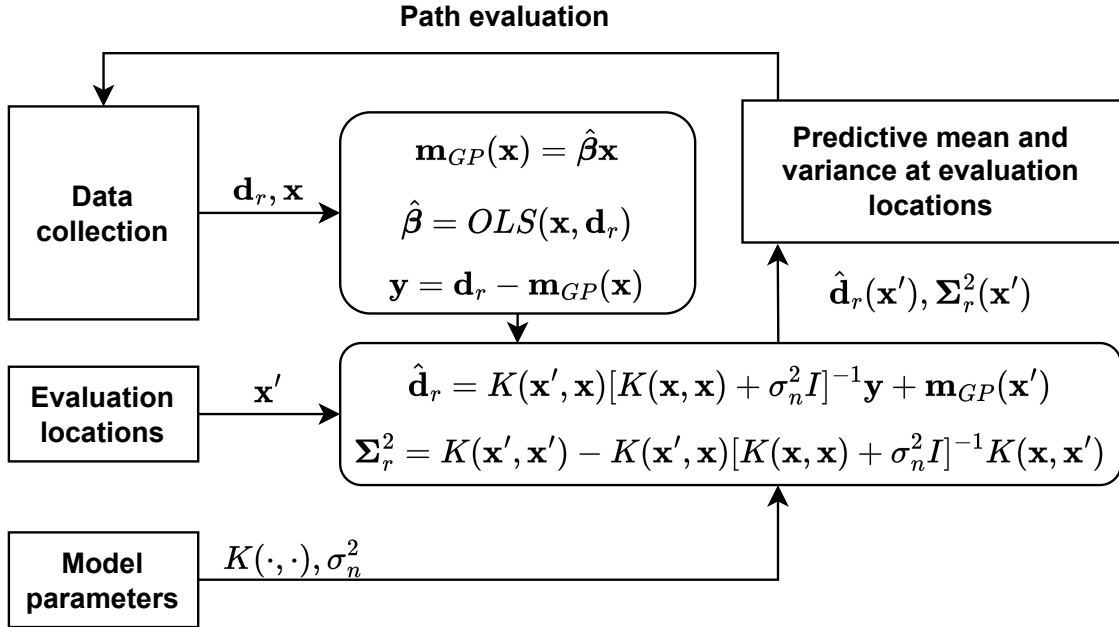


Figure 3: Flowchart representation of the GP model fitting and evaluation, where  $OLS(\cdot)$  is the *ordinary least squares regression*.

191 soft constraint on the directionality.

## 192 Evaluation points

193 In choosing which points to evaluate, we draw  $k$  concentric circles around vehicle's current position and draw  
 194  $j$  equally spaced points on each circle. The innermost circle has a radius of  $r_{inner}$  and the outermost circle  
 195 has a radius of  $r_{outer}$ . The radii of the intermediate circles, if  $k > 2$ , are drawn such that the square root of  
 196 each radius,  $r$ , is equidistant, as presented in Equation 11, where  $c$  is constant. The inner circles are closer  
 197 together than the outer ones, enabling a more detailed view of the immediate vicinity.

$$\sqrt{r_{i+1}} - \sqrt{r_i} = c \quad (11)$$

198 The generated  $j \times k$  evaluation points, as visible in Figure 4, where the parameters were set as in table 1.  
 199 The potential paths for the vehicle are developed and evaluated using the prediction from the GP for each  
 200 point.

Table 1: Evaluation points example values.

$k$	$j$	$r_{inner}$ [m]	$r_{outer}$ [m]
8	4	150	1000

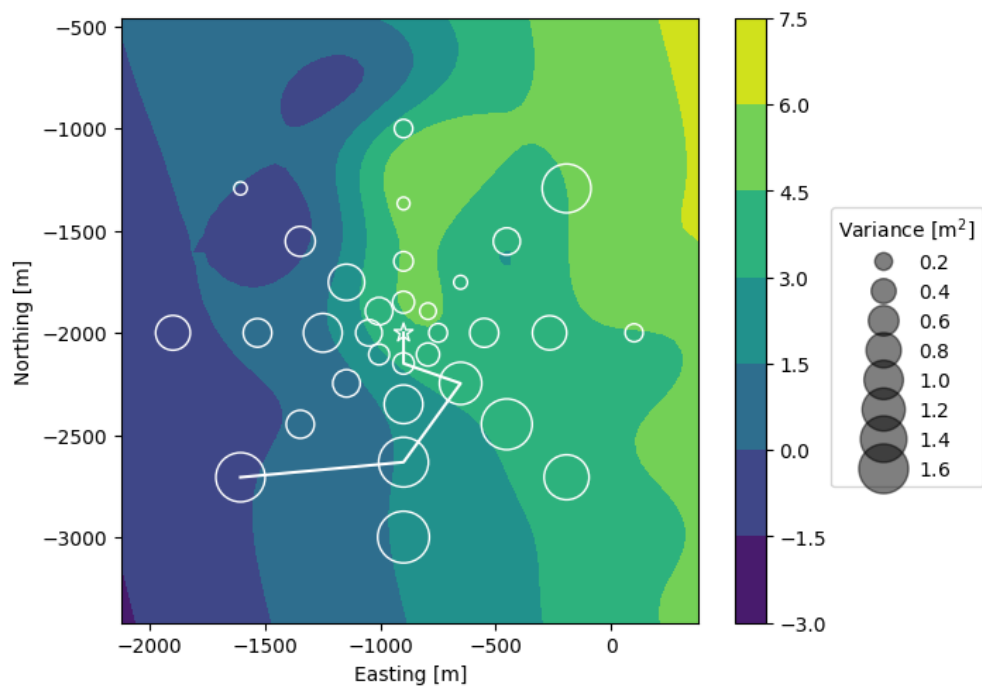


Figure 4: Example evaluation points for the GP, marked by circles, where the vehicle position is centered at [Northing, Easting]= [-2000, -900]m, marked by a star. The size of the circle indicates the standard deviation at that point,  $\Sigma_r$ , and the background contour plot and the colorbar indicate the predicted river plume depth,  $\hat{d}_r$  in meters. For visualization purposes the contour plot is generated over a grid evaluation of the GP, this is not done in the vehicle.

201 **Generation of potential paths**

202 After evaluating the estimated river depths,  $\hat{\mathbf{d}}_r$  and variances,  $\Sigma_r^2$  of  $\hat{\mathbf{d}}_r$  at the evaluation points,  $\mathbf{p}_e$ , a set of  
203 potential paths,  $P$ , can be generated. Each potential path  $\mathbf{p}_i$  is a vector of length  $k$ , containing the position  
204 of the evaluation points. The path is generated by choosing one point from each concentric circle in an  
205 orderly fashion until all possible combinations are generated; the maximum number of paths is then  $k^j$ . We  
206 prune the number of paths by limiting the angle,  $\psi$ , between the path's edges to keep the directionality in  
207 the evaluation. The path generation is only done once, and for each evaluation, or *update step*, the points are  
208 offset by the vehicle position. Only straight line paths will be generated if  $\psi$  is sufficiently small;  $\psi < \frac{k}{2\pi}$  [rad].  
209 By increasing the distance between the concentric circles, the first steps of the path are implicitly weighed  
210 the more than the last. One path, along with all evaluation pints,  $\mathbf{p}_e$ , at a update step is plotted in Figure  
211 4.

212 **2.5 Path evaluation**

213 When potential paths have been generated they can be evaluated in deliberation and the best path is chosen.  
214 We have chosen to evaluate based on three criteria: estimated river plume depth 1), uncertainty 2), and  
215 difference in estimated river plume depth from the estimated river plume depth at the current location 3).

216 Evaluation of the GP provides estimates of river plume depth 1), and positive contributions to the evaluation  
217 function in Equation (12). The constant  $k_r$  controls the influence of the estimated river plume depth for  
218 each evaluation point.

219 The uncertainty 2), or standard deviation,  $\Sigma_r$ , in the GP estimates also counts positive in the evaluation  
220 function; this favors exploration of new areas in addition to seeking regions of deeper river plume. The  
221 uncertainty is weighted by the constant  $k_u$ .

222 Weighting of the absolute value of the difference between the estimated river plume depth along the path  
223 and the estimated river plume depth at the current location 3) is a measure to explore the more shallow and  
224 even oceanic parts of the domain. By weighting the difference in plume depth between where the robot is  
225 and where it is planning to go, the robot seeks locations that are unlike the current location. This can be  
226 seen as a weighting of heterogeneity. The difference is weighted by the constant  $k_d$ . The intended effect is  
227 to draw the robot towards deeper river plume depths when it is in a region of shallow plume depth and vice  
228 versa, encouraging exploration of the entire plume, rather than only the deepest points.

229 The evaluation function evaluates each potential path, and the path with the highest score is chosen as the  
230 preferred path for the vehicle until the next update step. Thus the path chosen will be as presented in  
231 Equation 12.

$$\mathbf{p}^* = \underset{\mathbf{p}}{\operatorname{argmax}}(k_r \hat{\mathbf{d}}_r + k_u \Sigma_r + k_d |\hat{\mathbf{d}}_r - \hat{\mathbf{d}}_{rc}^k|) \quad (12)$$

232 As none of these paths will be followed to its end, it is essential to keep in mind their function: to guide the  
233 vehicle to more valuable data. It is necessary to update the path of the vehicle based on a model constantly  
234 updating. The parameters  $k_r$ ,  $k_u$ , and  $k_d$  must be set to balance end user needs and robot capabilities. This  
235 is best done using sufficiently accurate simulated data, able to resolve and represent the river plume.

236 **2.6 Implementation and development**

237 The method described in the above was implemented on an LAUV belonging to the Underwater Systems and  
238 Technologies Lab (LSTS) from the Faculty of Engineering of the University of Porto (FEUP), and developed  
239 using simulated salinity data of the Douro river plume outside Porto, Portugal from the Iberian Biscay Irish  
240 Ocean Analysis and Forecasting system [29].

241 The code was written in Python and communicated with the on-board operating system, DUNE: Unified  
242 Navigation Environment (DUNE) [30], using a communication bridge written in C++ and implemented in  
243 the Robot Operating System (ROS) [31], communicating with the Inter Module Communication message  
244 system of DUNE.

245 The method was developed and mainly tested using the built-in simulator of DUNE, with access to the  
246 simulated salinity data. After the development using the simulator, the method was modified and tested on-  
247 board the LAUV Xplore-1 belonging to the LSTS-FEUP. Testing continued with software and hardware in  
248 the loop tests before the code was deemed ready for deployment. Together, these factors made development  
249 and testing more straightforward, as we had access to realistic environmental data allowing rapid testing  
250 and verification of the results.

251 **3 Results**

252 In this section, results from the simulation and field trials results in the Douro river plume outside Porto,  
253 Portugal are presented. The tuning variables used in both the simulation and the field trials are presented  
254 in Table 2, while the mission-specific operator inputs for both simulation and field trials are presented in  
255 Table 3.

256 **3.1 Simulation**

257 The simulations of the performance of the described deliberate path planning algorithm represent a reference  
258 for the field experiment. In Figure 5, the pilot survey mission starts at the northernmost point and follows  
259 the "V" shaped pattern. The sample points in the pilot survey are further from each other due to the  
260 amplitude of the yoyo, that goes between the surface and  $d_{max}$ , as the vehicle has a fixed diving angle and  
261 thus a linear relationship between yoyo amplitude and distance travelled in one "yo". Meanwhile, the yoyo  
262 envelope is reduced when the vehicle is in the adaptive phase. In the horizontal plane, we see that the  
263 algorithm first draws the vehicle path North, then West, South, and Southeast, North, Northeast and East  
264 before re-encountering the plume, while in the plume, the vehicle behavior becomes more chaotic but follows  
265 the general trend of exploring southward before ending the mission in the Southeastern corner. The GP  
266 model realization of the predicted river plume depth, over the area covered by the AUV is plotted along with  
267 its variance and the sampling locations in Figure 5.

268 In the left panel of Figure 7, the simulated salinity field measurements from below 0.5m is plotted, and  
269 shows more variation in the salinity closer to the surface, as well as somewhat chaotic NCSR and  $\frac{\partial}{\partial d}$ NCSR  
270 in the middle and right panel. The upper 0.5m of data is removed to avoid a bias since there are many  
271 more surface measurements than measurements at depth. This leaves the measurements distributed more  
272 uniformly along the vertical profile. In the upper region of the left panel, the salinities span from < 28 to 36,  
273 while at 7m depth, there is less of a span. From the middle and right hand panels the NCSR and  $\frac{\partial}{\partial z}$ NCSR  
274 are visible, and seem to exhibit a chaotic behavior. The estimated river plume depth, measured river plume  
275 depth and the estimation error are plotted in Figure 6; here, we can see that the measurements,  $\mathbf{d}_r$ , are  
276 noisy compared to the estimates. The noisy data lead to a higher value for  $\sigma_f$  during the last part of the  
277 mission, increasing the yoyo-envelope.

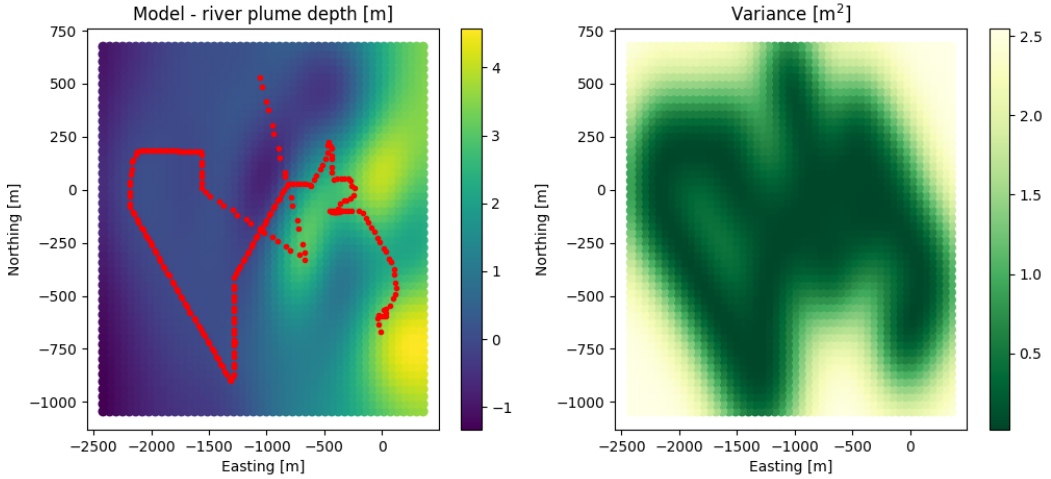


Figure 5: Model and variance of the simulated river plume depth, as collected during the mission simulation. The red dots represent the sample locations, while the color map indicates the estimated river plume depth for the left panel and uncertainty for the right panel.

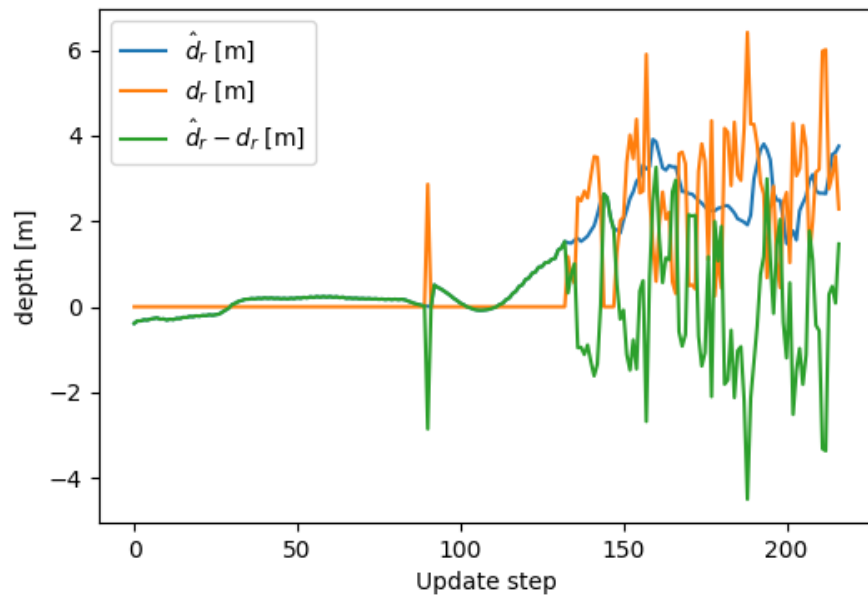


Figure 6: Estimated river plume depth,  $\hat{d}_r$ , measured river plume depth,  $d_r$ , and error in estimation,  $\hat{d}_r - d_r$ , for each update step during the adaptive phase during the simulation.

Table 2: Common tuning variables for the simulation and field trials.

Variable	Value	Explanation
$n_{knots}$	6	Number of knots in the <i>NCSR</i>
$\alpha$	0.2	Low pass filter constant
$l$	300m	Length scale in the kernel
$\sigma_n$	1.25m	Nugget effect standard deviation
$\sigma_{fmin}$	1.5m	Depth minimum standard deviation
$r_{inner}$	50m	Inner radius of evaluation points
$r_{outer}$	2000m	Outer radius of evaluation points
$j$	4	Number of concentric circles of evaluation points
$k$	8	Number of points on each circle of evaluation points
$k_r$	4.0	Weight of the estimated depth in the path score
$k_u$	1.5	Weight of the uncertainty in the path score
$k_d$	1.5	Weight of the difference of depths from current depth estimate

Table 3: Simulation and field trial specific user inputs for the simulated and the field trial runs.

Variable	Simulation	Field trials	Explanation
$s_0$	28	34.5	Minimum salinity for oceanic/mixed water
$s_r$	33	35.5	Maximum value for river/mixed water
$d_{max}$	7m	7m	Maximum depth allowed for mission
$p_{start}$	[41.1453N, -8.6968E]	[41.1341N, -8.6977E]	Starting position of the pilot survey
$l_{ps}$	1000m	1000m	Length of the pilot survey transects
$[\theta_0, \theta_1]$	[155°, 290°]	[155°, 290°]	Headings of the pilot survey transects

### 278 3.2 Field trials

- 279 The field trials were conducted on Friday, November 5th, 2021, in the Douro river plume outside Porto,  
 280 Portugal. The LAUV Xplore-1 was programmed by the operator to collect data using the inputs presented  
 281 in Table 3. The pilot survey started at 15:35 local time, and the adaptive mission ended at 17:58. The  
 282 mission track is plotted in Figure 8 over a satellite image taken earlier the same day at 11:30, showing the  
 283 surrounding operational area. The tidal peak was at 14:46, and it is assumed that the plume visible in Figure  
 284 8 was formed during the previous ebb in tide, and the plume identified by the AUV is the subsequent plume  
 285 forming. The data model used, Iberian Biscay Irish Ocean Analysis and Forecasting system [29], showed a  
 286 surface current from the North following the coastline and pushing the river plume to the South-East.  
 287 Data collected by the vehicle showed that the river plume was crossed horizontally and vertically several  
 288 times during the operations, as can be seen in Figure 8. The mission data shows that the AUV was able to  
 289 generate a model, assimilate data online, and act upon it to return to the river plume.  
 290 The vehicle sample locations are plotted along with the GP predictive mean,  $\hat{d}_r$ , over the operational area

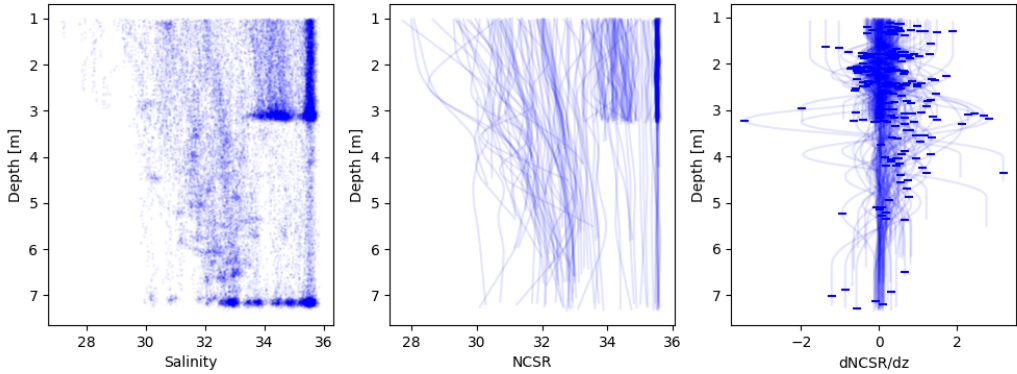


Figure 7: Salinity measurements, NCSR profiles and their differentiation, for the complete simulated mission. Maximum of absolute value of differentiation marked in right panel by tick-marks.

and variance in right panel,  $\Sigma_r$ , in Figure 9. The starting position corresponds with the northernmost sample location, and here the pilot survey "V" is also visible, as it was for the simulation. The sampling is not as continuous as the simulation; this is due to the vehicle stopping after encountering a wave and being restarted.

As seen from the maximum and minimum salinity values in Table 3, the oceanic water was closer in salinity to the river plume waters than in the simulation. The upper 4m is dominated by two distinct water masses, one with salinity around 35.1, and one with salinity around 35.7 shown in the left panel in Figure 11. The waters below 5m appear to be more homogeneous, both in temperature and salinity. In the middle and right panel of Figure 11, the NCSR and  $\frac{\partial}{\partial d}$ NCSR are plotted, and these seem more structured than the simulated profiles.

The estimated river plume depth, measured river plume depth and the estimation error are plotted in Figure 12, here, the estimates can predict the measurements to a more significant degree than in the simulation. This observation can be explained by the stratification visible in Figure 11 around 4 to 5m; it is also here that most measurements of the river plume depth is observed, while in the plume, as seen in Figure 10.

The timeline of the vehicle depth, river plume depth measurements and the yoyo-envelope associated with each measurement is plotted in Figure 10. In the later half of the mission, the yoyo-envelope follows the depth of the river plume, and both plume depth and envelope stabilizes. The vertical range of the vehicle path is observed to be smaller than the desired path in the yoyo-envelope. This can be explained by the vehicle's acceptance radius around waypoints, which is one meter in the z-direction.

The scores of the winning paths, the elements of Equation (12), and direction of travel is presented in Figure

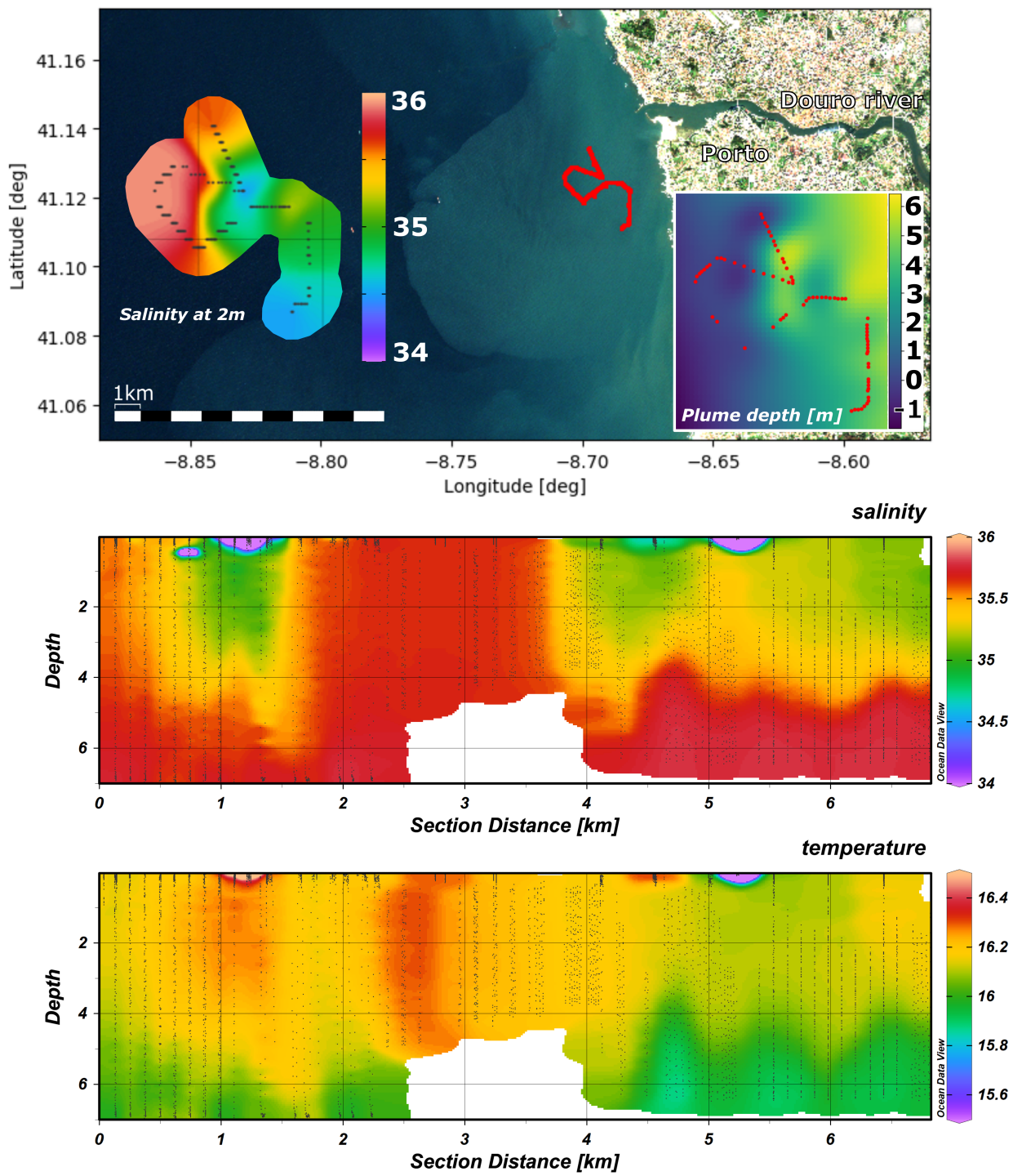


Figure 8: Mission track, in red, overlaid on a satellite image taken by the Sentinel-2A at 11:30 UTC on Friday, November 5th 2021. The Douro river is visible in the upper right of the image, as well as a plume of turbid water from the river associated with a larger river flow in the autumn. Left panel: salinity data at 2 meters depth collected during the sea trials showing two different water masses. Right panel: model predicted river plume depth. Lower panel: salinity and temperature vertical slice from the data collected by the vehicle. Black dots represent the trajectory followed by the vehicle.

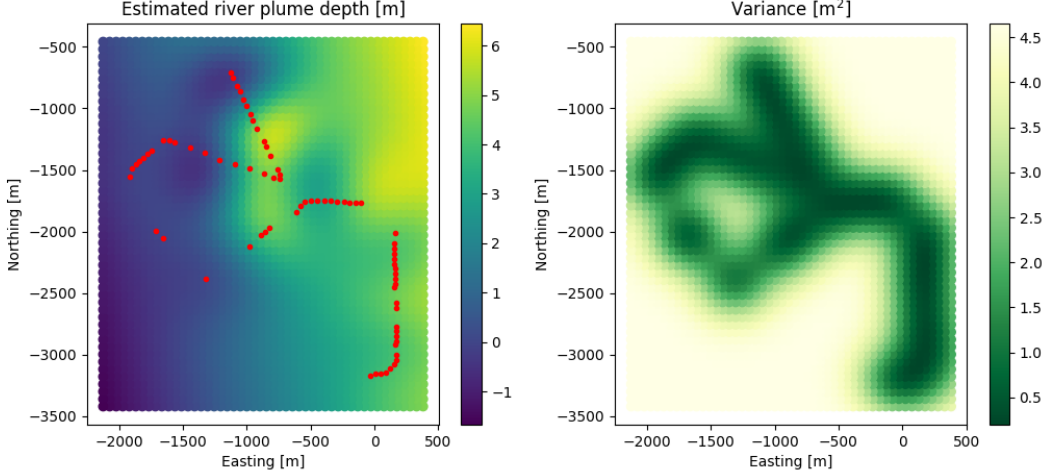


Figure 9: Model and variance of the river plume depth, as collected during the field trials. The red dots represent the sample locations while the color map indicates the estimated river plume depth and the uncertainty thereof in the right panel.

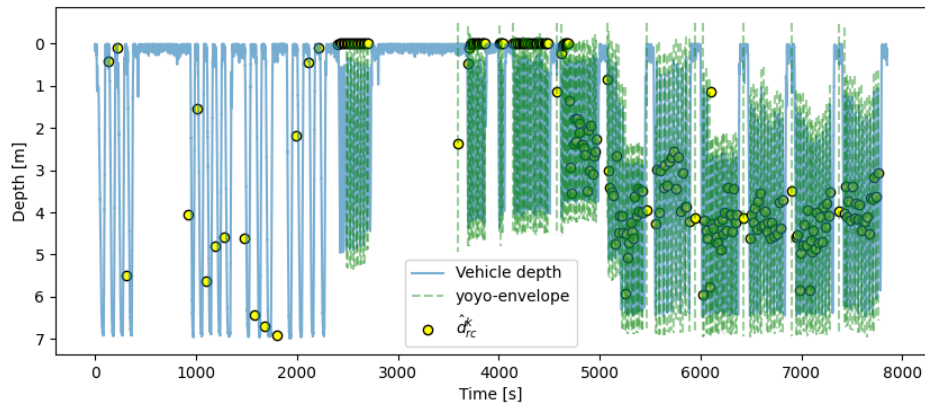


Figure 10: Vehicle depth, yoyo-envelope and estimated river plume depth at time step  $k$ ,  $\hat{d}_{rc}^k$ , plotted against time since mission start. Recorded vehicle depth [m] is plotted in pale blue, yoyo-envelope for each plume depth estimate is plotted as a dashed green line, and  $\hat{d}_{rc}^k$  [m] is plotted as yellow circles outlined in black.

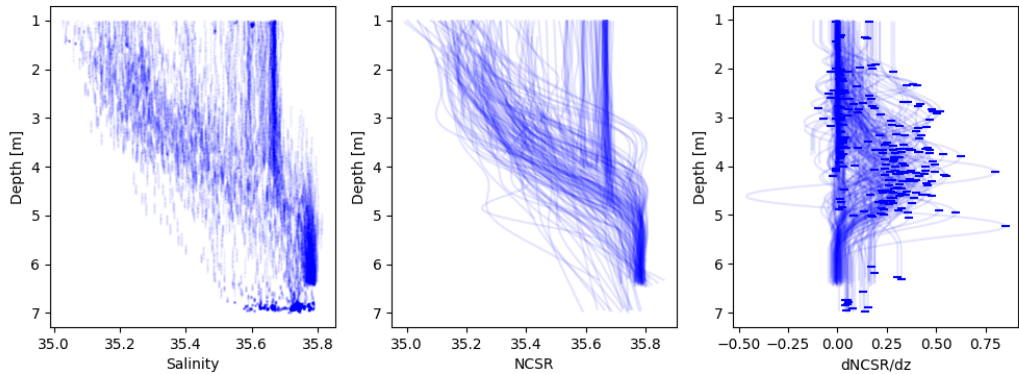


Figure 11: Salinity measurements, NCSR profiles and their differentiation, for the entirety of the mission. Maximum of absolute value of differentiation marked in right panel by tick-marks.

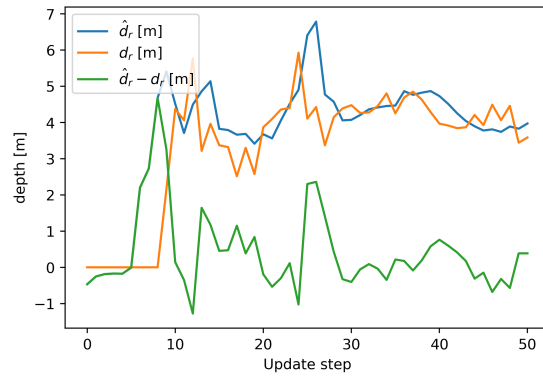


Figure 12: Estimated river plume depth, measured river plume depth and error in estimation for each update step during the adaptive phase.

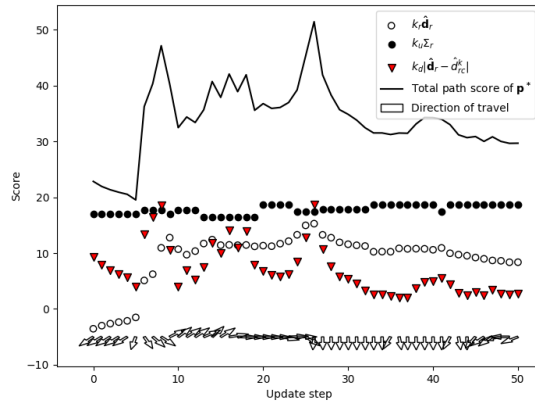


Figure 13: Scores of the different elements and total of the best path from Equation (12) during the adaptive phase.

311 13. Here the last element,  $k_d|\hat{d}_r - \hat{d}_{rc}^k|$ , is the most dynamic, driving the decision making along with the first  
312 element  $k_r\hat{d}_r$ . The uncertainty element,  $k_u\Sigma_r$  remains fairly constant through the adaptive phase, pushing  
313 the path to areas of high uncertainty. In comparing Figures 12 and 13, it is evident that the exploration  
314 element dominates the path evaluation dynamic when measurements are erratic.

315 **4 Discussion**

316 The results have shown the proposed method at work on both simulated and field data. Showing the ability  
317 identify and return to the river plume region by the adaptive agent. In this section the following is discussed;  
318 river plume depth estimation, GP model, evaluation points generation, and tuning.

319 **4.1 Plume depth estimation**

320 The measurement or estimation of the river plume depth by Equation 1 was shown to work better in  
321 cases where the ocean exhibits intense vertical stratification. This difference is visible when comparing the  
322 performance of the algorithm in simulation and field trials, comparing Figures 6 and 12. In the simulation  
323 trials, the vertical stratification was weak, and the variance in the salinity data was more prominent in the  
324 horizontal plane. In the field trials, we see a much more stratified waters, albeit less varied. In cases with  
325 no to weak stratification, the gradient method used herein will not work properly, and the data become  
326 noisy, as seen in Figures 6 and 7. In the cases of a weak but detectable signal, one can employ a more strict  
327 low-pass filter to estimate the current river plume depth and increase the nugget variance,  $\sigma_\tau$  in the model.  
328 For robustness, one could add a threshold to the maximum value of  $|\frac{\partial}{\partial} \text{NCSR}|$ , and reject measurements that  
329 fall below the threshold.

330 **4.2 Gaussian process model**

331 Using a linear regression for the  $m_{GP}(\cdot)$ -function in a GP without a bounding box could give extreme values  
332 at the outermost evaluation points. This gap could be remedied by clamping the output between the surface  
333 and  $d_{max}$ . The residual in this case will also not be Gaussian, since there are many measurements where  
334 the estimated river plume depth is 0m, and  $d_{max}$  if clamped, as seen in Figures 7 and 12. One could also  
335 attempt to only evaluate the GP inside the plume by estimating the horizontal plume extent [15]. By not  
336 covering the edges along any operational area, the GP might estimate erratic values with high variance at  
337 far away locations.

338 **4.3 Evaluation points**

339 One criticism of the evaluation point and potential path generation can be that we chose a too large outer  
340 radius, such that the path score become vulnerable to bias incurred by the model,  $m_{GP}(\cdot)$ , as discussed

341 above. Further the points need to be generated and evaluated at every update step. To mitigate a large  
342 computational cost, the number of potential waypoints can be limited by the user. In the field trials, the  
343 number of waypoints were  $8 \times 4 = 32$  and the number of measurements were sufficiently small, allowing for  
344 quick computation and adaption for the available hardware.

345 **4.4 Tuning**

346 In both the simulation and field trials, the AUV first moves in the open ocean before entering the river plume  
347 and does not exit the plume during the rest of the mission. By increasing the  $k_d$ -gain, we could reward the  
348 movement towards border regions. Otherwise, the tuning used proved sufficient for finding and exploring  
349 the plume without getting stuck at local river plume maxima. Neither was the vehicle drawn too much  
350 to regions of high uncertainty, but low estimated river plume depth, something that might happen if the  
351 river plume is not detected in the pilot-survey. The AUV path has similar features in both simulation and  
352 field trials, this is caused by the use of the same model parameters and data-driven path finding algorithm.  
353 Further, the simulated data field tries to emulate the river plume. By first turning West, then returning to  
354 the plume, it is shown that the vehicle is able to adapt to the plume location in both cases.

355 **4.5 Temporal effects**

356 From Figure 8, we can see that there are larger-scale effects that can be measured, and in this river plume,  
357 there seems to be a tidally driven component. If one were to do a longer-term deployment of river plume  
358 mapping ( $> 3$  hours or  $\frac{1}{4}$ <sup>th</sup> tidal cycle), the effects of the tide should be taken into account, either driven by  
359 model data or simply by propagating uncertainty temporally as described in [13].

360 **5 Conclusion and further work**

361 In this paper, a method for adaptive tracking salinity gradients based on Gaussian process and a lightweight  
362 ocean model for an AUV was presented, with field results from the Douro river plume outside Porto, Portugal.  
363 The method models the river plume depth, inferred by analysis of each the vertical profiles of the salinity  
364 measurements made by the undulating vehicle. After an initial pre-programmed pilot survey, ending in the  
365 open ocean water, the vehicle returned to the river plume for further mapping and exploration. Due to  
366 path optimization using estimated plume depth, uncertainty and the heterogeneity of salinity measurements  
367 along the path compared to the current location, the AUV was able to detect, explore, and measure the river  
368 plume for the duration of the mission. The salinity measurements exhibited a strong vertical gradient signal  
369 within the river plume. Separating the adaption in two parts, horizontal and vertical, enables a sparse set of  
370 measurements by using the vertical profiles as measurements, rather than salinity measurements directly. The  
371 boundless approach was shown to let the vehicle pursue and investigate the river plume without discernible  
372 drawbacks. This enabled the freedom from a bounded grid-based method traditionally associated with GPs  
373 for adaptive sampling in the ocean. In future missions, adding a temporal component to the model is  
374 advised, degrading measurements as they age due to tidal forcing and other unmodelled processes such as  
375 wind and current. In addition, rejecting weak gradient measurements should be considered. Further work  
376 also includes a more formal configuration of the path-finding parameters in Equation (12), optimizing for  
377 the desired behavior in a multitude of plume scenarios.

378 **Acknowledgments**

379 The research presented in this paper was funded by the Research Council of Norway through the Nansen  
380 Legacy project RCN #276730, the Center of Excellence Autonomous Marine Operations and Systems  
381 (AMOS), RCN #223254, and the European Union’s Horizon 2020 Marine robotics research infrastructure  
382 network project under grant agreement No 731103. A big thanks to Maria Costa then at Underwater Systems  
383 and Technology Laboratory (LSTS) at the Engineering Faculty of University of Porto (FEUP), Portugal, for  
384 help with integration and testing. Many thanks to BBDouro’s skippers who perfectly ran boat operations  
385 during the tests.

386 **References**

- 387 [1] C Brock Woodson and Steven Y Litvin. Ocean fronts drive marine fishery production and biogeochemical  
388 cycling. *Proceedings of the National Academy of Sciences*, 112(6):1710–1715, 2015.
- 389 [2] SV Prants. Marine life at lagrangian fronts. *Progress in Oceanography*, page 102790, 2022.
- 390 [3] Rainer Lohmann and Igor M Belkin. Organic pollutants and ocean fronts across the atlantic ocean: A  
391 review. *Progress in Oceanography*, 128:172–184, 2014.
- 392 [4] José Pinto, Renato Mendes, José CB da Silva, Joao M Dias, and Joao Borges de Sousa. Multiple  
393 autonomous vehicles applied to plume detection and tracking. In *2018 OCEANS-MTS/IEEE Kobe  
394 Techno-Oceans (OTO)*, pages 1–6. IEEE, 2018.
- 395 [5] R Mendes, N Vaz, D Fernández-Nóvoa, JCB Da Silva, M Decastro, M Gómez-Gesteira, and JM Dias.  
396 Observation of a turbid plume using modis imagery: The case of douro estuary (portugal). *Remote  
397 sensing of environment*, 154:127–138, 2014.
- 398 [6] Diogo Teixeira, João Borges de Sousa, Renato Mendes, and Joana Fonseca. 3d tracking of a river plume  
399 front with an auv. In *OCEANS 2021: San Diego – Porto*, pages 1–9, 2021.
- 400 [7] Conor McGann, Frederic Py, Kanna Rajan, Hans Thomas, Richard Henthorn, and Rob McEwen. T-  
401 rex: A model-based architecture for auv control. In *3rd Workshop on Planning and Plan Execution for  
402 Real-World Systems*, volume 2007, 2007.
- 403 [8] Yanwu Zhang, John P Ryan, James G Bellingham, Julio BJ Harvey, and Robert S McEwen. Autonomous  
404 detection and sampling of water types and fronts in a coastal upwelling system by an autonomous  
405 underwater vehicle. *Limnology and Oceanography: Methods*, 10(11):934–951, 2012.

- 406 [9] Yanwu Zhang, James G Bellingham, John P Ryan, Brian Kieft, and Michael J Stanway. Two-  
407 dimensional mapping and tracking of a coastal upwelling front by an autonomous underwater vehicle.  
408 In *2013 OCEANS-San Diego*, pages 1–4. IEEE, 2013.
- 409 [10] Yanwu Zhang, James G Bellingham, John P Ryan, Brian Kieft, and M Jordan Stanway. Autonomous  
410 four-dimensional mapping and tracking of a coastal upwelling front by an autonomous underwater  
411 vehicle. *Journal of Field Robotics*, 33(1):67–81, 2016.
- 412 [11] Yanwu Zhang, Brian Kieft, Brett W Hobson, John P Ryan, Benedetto Barone, Christina M Preston,  
413 Brent Roman, Ben-Yair Raanan, Roman Marin III, Thomas C O'Reilly, et al. Autonomous tracking and  
414 sampling of the deep chlorophyll maximum layer in an open-ocean eddy by a long-range autonomous  
415 underwater vehicle. *IEEE Journal of Oceanic Engineering*, 2019.
- 416 [12] Stephanie Kemna. *Multi-robot strategies for adaptive sampling with autonomous underwater vehicles*.  
417 PhD thesis, University of Southern California, 2018.
- 418 [13] Trygve OIav Fossum. *Adaptive Sampling for Marine Robotics*. PhD thesis, Norwegian University of  
419 Science and Technology, 2019.
- 420 [14] Trygve Olav Fossum, Petter Norgren, Ilker Fer, Frank Nilsen, Zoe Charlotte Koenig, and Martin Lud-  
421 vigsen. Adaptive sampling of surface fronts in the arctic using an autonomous underwater vehicle. *IEEE*  
422 *Journal of Oceanic Engineering*, 2021.
- 423 [15] Trygve Olav Fossum, Cédric Travelletti, Jo Eidsvik, David Ginsbourger, and Kanna Rajan. Learning  
424 excursion sets of vector-valued gaussian random fields for autonomous ocean sampling. *The Annals of*  
425 *Applied Statistics*, 15(2):597–618, 2021.
- 426 [16] Paul Stankiewicz, Yew T Tan, and Marin Kobilarov. Adaptive sampling with an autonomous underwater  
427 vehicle in static marine environments. *Journal of Field Robotics*, 38(4):572–597, 2021.
- 428 [17] Glaucia M Fragoso, Emlyn J Davies, Trygve O Fossum, Jenny E Ullgren, Sanna Majaneva, Nicole  
429 Aberle, Martin Ludvigsen, and Geir Johnsen. Contrasting phytoplankton-zooplankton distributions  
430 observed through autonomous platforms, in-situ optical sensors and discrete sampling. *Plos one*,  
431 17(9):e0273874, 2022.
- 432 [18] Rodney Brooks. A robust layered control system for a mobile robot. *IEEE journal on robotics and*  
433 *automation*, 2(1):14–23, 1986.
- 434 [19] Mae L Seto. *Marine robot autonomy*. Springer Science & Business Media, 2012.
- 435 [20] Jimin Hwang, Neil Bose, and Shuangshuang Fan. Auv adaptive sampling methods: A review. *Applied*  
436 *Sciences*, 9(15):3145, 2019.

- 437 [21] Carl Edward Rasmussen. Gaussian processes in machine learning. In *Summer School on Machine*  
438 *Learning*, pages 63–71. Springer, 2003.
- 439 [22] Gunhild Elisabeth Berget, Trygve Olav Fossum, Tor Arne Johansen, Jo Eidsvik, and Kanna Rajan.  
440 Adaptive sampling of ocean processes using an auv with a gaussian proxy model. *IFAC-PapersOnLine*,  
441 51(29):238–243, 2018.
- 442 [23] Thomas H Cormen, Charles E Leiserson, Ronald L Rivest, and Clifford Stein. *Introduction to algorithms*.  
443 MIT press, 2009.
- 444 [24] Trygve Olav Fossum, Jo Eidsvik, Ingrid Ellingsen, Morten Omholt Alver, Glauca Moreira Fragoso, Geir  
445 Johnsen, Renato Mendes, Martin Ludvigsen, and Kanna Rajan. Information-driven robotic sampling  
446 in the coastal ocean. *Journal of Field Robotics*, 35(7):1101–1121, 2018.
- 447 [25] Sergey Frolov, Bartolome Garau, and James Bellingham. Can we do better than the grid survey: Opti-  
448 mal synoptic surveys in presence of variable uncertainty and decorrelation scales. *Journal of Geophysical*  
449 *Research: Oceans*, 119(8):5071–5090, 2014.
- 450 [26] Tore Mo-Bjørkelund, Trygve O Fossum, Petter Norgren, and Martin Ludvigsen. Hexagonal grid graph  
451 as a basis for adaptive sampling of ocean gradients using auvs. In *Global Oceans 2020: Singapore–US*  
452 *Gulf Coast*, pages 1–5. IEEE, 2020.
- 453 [27] Trygve O Fossum, Glauca M Fragoso, Emlyn J Davies, Jenny E Ullgren, Renato Mendes, Geir Johnsen,  
454 Ingrid Ellingsen, Jo Eidsvik, Martin Ludvigsen, and Kanna Rajan. Toward adaptive robotic sampling  
455 of phytoplankton in the coastal ocean. *Science Robotics*, 4(27), 2019.
- 456 [28] Jo Eidsvik, Tapan Mukerji, and Debarun Bhattacharjya. *Value of information in the earth sciences:*  
457 *Integrating spatial modeling and decision analysis*. Cambridge University Press, 2015.
- 458 [29] Claire Maraldi, J Chanut, Bruno Levier, Nadia Ayoub, Pierre De Mey, G Reffray, Florent Lyard, Sylvain  
459 Cailleau, Marie Drévillon, EA Fanjul, et al. Nemo on the shelf: assessment of the iberia–biscay–ireland  
460 configuration. *Ocean Science*, 9(4):745–771, 2013.
- 461 [30] Alexandre Sousa, Luis Madureira, Jorge Coelho, José Pinto, João Pereira, João Borges Sousa, and  
462 Paulo Dias. Lauv: The man-portable autonomous underwater vehicle. *IFAC Proceedings Volumes*,  
463 45(5):268–274, 2012.
- 464 [31] Morgan Quigley, Ken Conley, Brian Gerkey, Josh Faust, Tully Foote, Jeremy Leibs, Rob Wheeler, and  
465 Andrew Y Ng. Ros: an open-source robot operating system. In *ICRA workshop on open source software*,  
466 page 5. Kobe, Japan, 2009.